

Electronic Supplementary Information for

Single-Ion Magnet behaviour in homoleptic Co(II) complexes bearing 2-iminopyrrolyl ligands

Patrícia S. Ferreira,^a Ana C. Cerdeira,^b Tiago F. C. Cruz,^a Nuno A. G. Bandeira,^{*c} David Hunger,^d Alexander Allgaier,^d Joris van Slageren,^{*d} Manuel Almeida,^b Laura C. J. Pereira,^{*b}
Pedro T. Gomes^{*a}

^a Centro de Química Estrutural, Institute of Molecular Sciences, Departamento de Engenharia Química, Instituto Superior Técnico, Universidade de Lisboa, Av. Rovisco Pais 1, 1049-001 Lisboa, Portugal.

^b Centro de Ciências e Tecnologias Nucleares, Departamento de Engenharia e Ciências Nucleares, Instituto Superior Técnico, Universidade de Lisboa, 2695-066 Bobadela LRS, Portugal.

^c BioISI - Biosystems & Integrative Sciences Institute, Departamento de Química e Bioquímica, Faculdade de Ciências, Universidade de Lisboa, Campo Grande, Ed. C8, 1749-016 Lisboa, Portugal.

^d Institut für Physikalische Chemie, Universität Stuttgart, Pfaffenwaldring 55, Stuttgart D-70569, Germany.

Table of Contents

FTIR and ¹ H NMR spectra of complex 4	S2
Effective magnetic moments in solution and in solid state of complexes 1-4	S3
Powder X-ray diffraction of complexes 1-4	S4
Selected bond distances and angles for complexes 1-4	S6
Crystallographic data for complex 4	S7
Static (dc) magnetic measurements for complexes 1-3	S8
High-Frequency EPR (HF-EPR) of complexes 1-4	S10
Computational analysis	S13
Dynamic (ac) magnetic measurements for complexes 1-4	S19

FTIR and ^1H NMR spectra of complex **4**

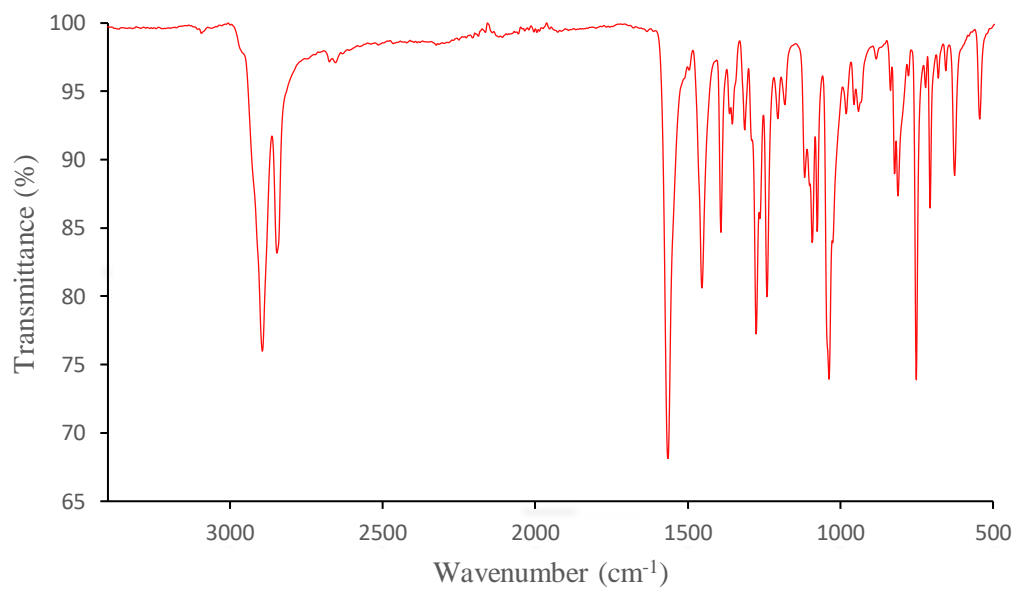


Figure S1. FTIR spectrum of complex **4**.

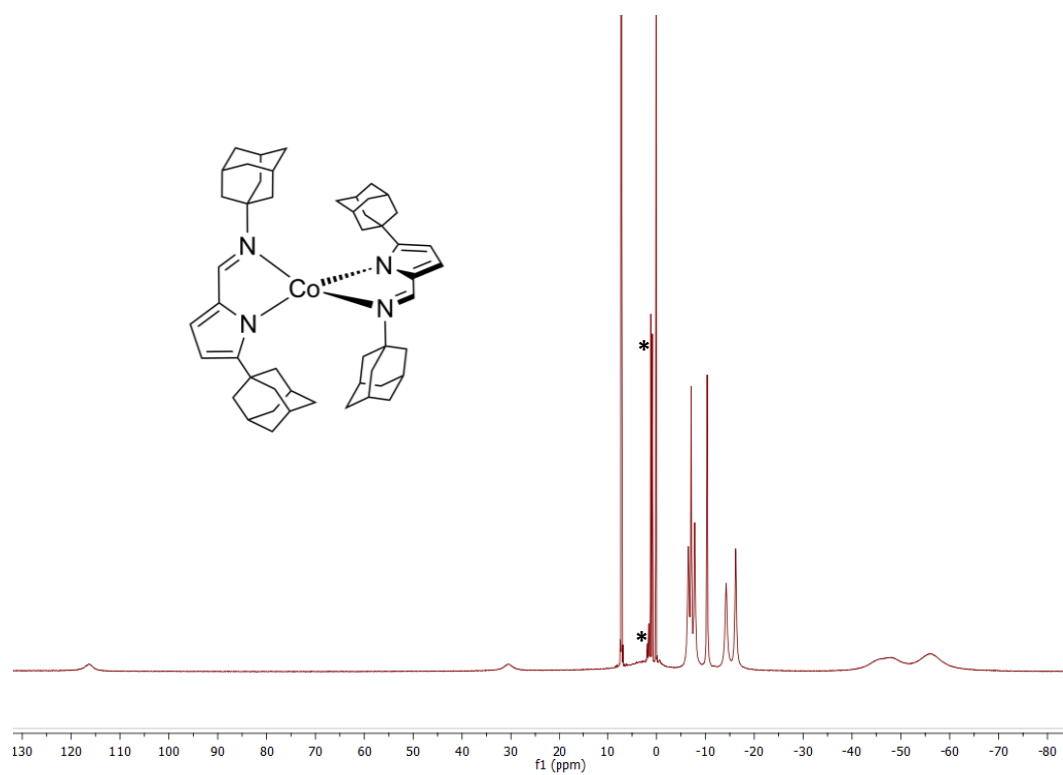


Figure S2. ^1H NMR spectrum (300 MHz, C_6D_6) of **4**. The resonances denoted with asterisks (*) correspond to residual *n*-hexane.

Effective magnetic moments in solution and in solid state of complexes 1-4

Table S1. Effective magnetic moments μ_{eff} (μ_B) measured in toluene- d_8 solution (Evans method) and in solid state (SQUID method), at r.t. for complexes **1-4**.

Complex	μ_{eff} (μ_B)		Ref.
	<i>solution</i>	<i>solid state</i>	
1	4.2	3.85 ^a	17
2	4.8	4.79	18
3	5.0	4.50	18
4	4.7	5.13	<i>this work</i>

^a measured by the dc Extraction method

Powder X-ray diffraction of complexes 1-4

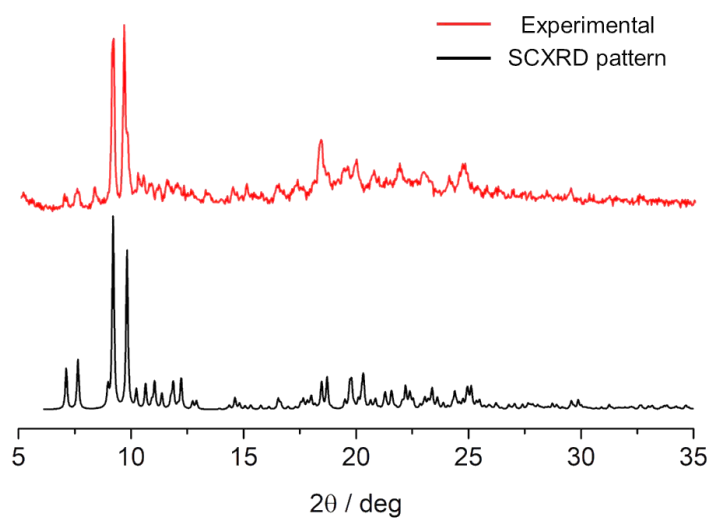


Figure S3. Comparison of the experimental X-ray powder diffraction of complex **1** (top) with X-ray diffraction pattern generated from the SCXRD data (bottom).

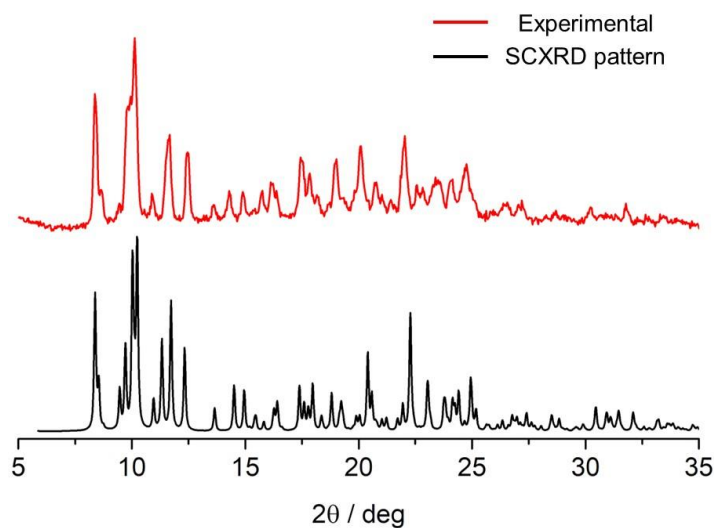


Figure S4. Comparison of the experimental X-ray powder diffraction of complex **2** (top) with X-ray diffraction pattern generated from the SCXRD data (bottom).

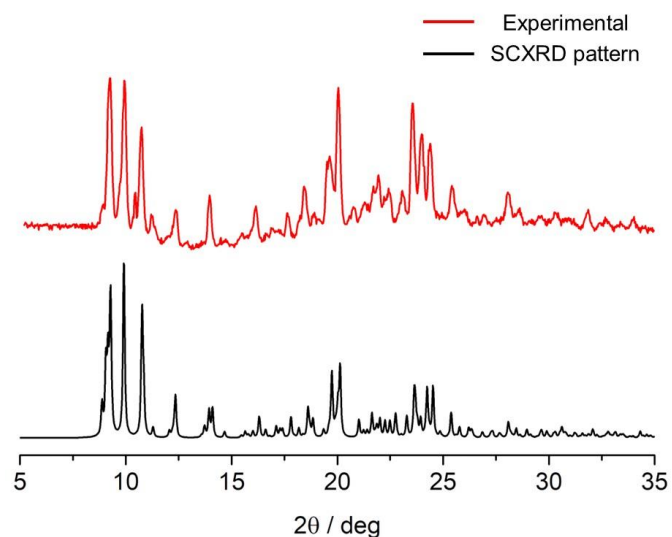


Figure S5. Comparison of the experimental X-ray powder diffraction of complex **3** (top) with X-ray diffraction pattern generated from the SCXRD data (bottom).

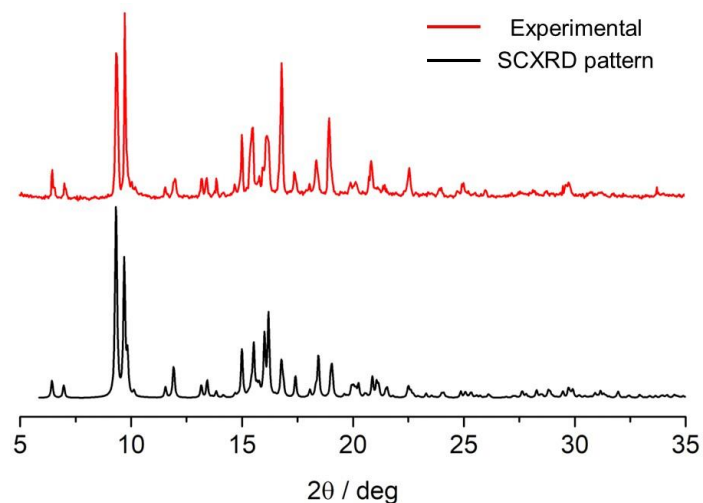


Figure S6. Comparison of the experimental X-ray powder diffraction of complex **4** (top) with X-ray diffraction pattern generated from the SCXRD data (bottom).

Selected bond distances and angles for complexes 1-4

Table S2. Selected bond distances (Å) and bond angles (°), chelating ligands bite angles θ , dihedral angles ϕ , interligand angles ω and parameters τ_4 for complexes **1-4**. The experimental values of the zero-field splitting parameter D are also presented in the last row for direct comparison.

	1 ^a		2 ^b	3 ^b	4
	<i>molecule #1</i>	<i>molecule #2</i>			<i>this work</i>
<i>Distances (Å)</i>					
Co-N1	1.985(9)	1.961(8)	1.976(3)	1.990(2)	1.979(2)
Co-N2	2.060(8)	2.054(8)	2.037(3)	2.031(2)	2.036(2)
Co-N3	1.971(8)	1.952(8)	1.983(3)	2.000(2)	1.979(2)
Co-N4	2.055(8)	2.034(7)	2.039(4)	2.039(2)	2.038(2)
<i>Angles (°)</i>					
N1-Co-N3	120.2(4)	125.2(4)	119.0(1)	114.90(7)	116.67(9)
N2-Co-N4	119.0(3)	114.6(3)	120.0(1)	125.95(7)	124.51(9)
N1-Co-N4	126.0(3)	125.9(3)	128.7(2)	125.01(7)	124.85(10)
N3-Co-N2	132.4(3)	130.1(3)	127.1(1)	126.23(7)	126.18(10)
N1-Co-N2 (θ_1) ^c	82.5(3)	83.0(3)	83.8(1)	84.15(7)	84.63(10)
N3-Xo-N4 (θ_2) ^c	82.8(3)	83.4(3)	83.91(14)	85.11(7)	84.8(1)
Dihedral ϕ ^d	81.03(3)	82.00(4)	82.20(17)	84.68(8)	85.2(1)
Angle ω ^e	173.5(2)	174.7(2)	177.12(12)	162.42(5)	170.61(6)
Parameter τ_4 ^f	0.72	0.74	0.74	0.76	0.77
D (cm ⁻¹) (exp.)	-69(5)		-53(4)	-48(3)	-52(4)

^a Ref. 17; ^b Ref. 18; ^c θ_1 and θ_2 = N-Co-N chelating ligands bite angles; ^d ϕ = dihedral angle formed between planes defined by atoms (Co, N1, N2) and (Co, N3, N4); ^e ω = interligand angle formed between dummy bonds Co-centroid (C2-C6) and Co-centroid (C27-C31); ^f Ref. 23.

Crystallographic data for complex 4

Table S3. Crystallographic data for complex 4.

Formula	C ₅₀ H ₆₆ CoN ₄
M	781.99
λ (Å)	0.71073
T (K)	150
Crystal system	Monoclinic
Space group	P 21/c
a (Å)	12.2261(5)
b (Å)	12.9194(5)
c (Å)	26.3835(13)
α (Å)	90
β (Å)	92.773(2)
γ (Å)	90
V (Å ³)	4162.5(3)
Z	4
ρ_{calc} (g.cm ⁻³)	1.248
μ (mm ⁻¹)	0.452
Crystal size	0.150×0.080×0.080
θ_{max} (°)	25.738
Total data	19742
Unique data	7905
R _{int}	0.0695
R [$I > 2\sigma(I)$]	0.0541
R _w	0.1107
Goodness of fit	1.022

Static (dc) magnetic measurements for complexes 1-3

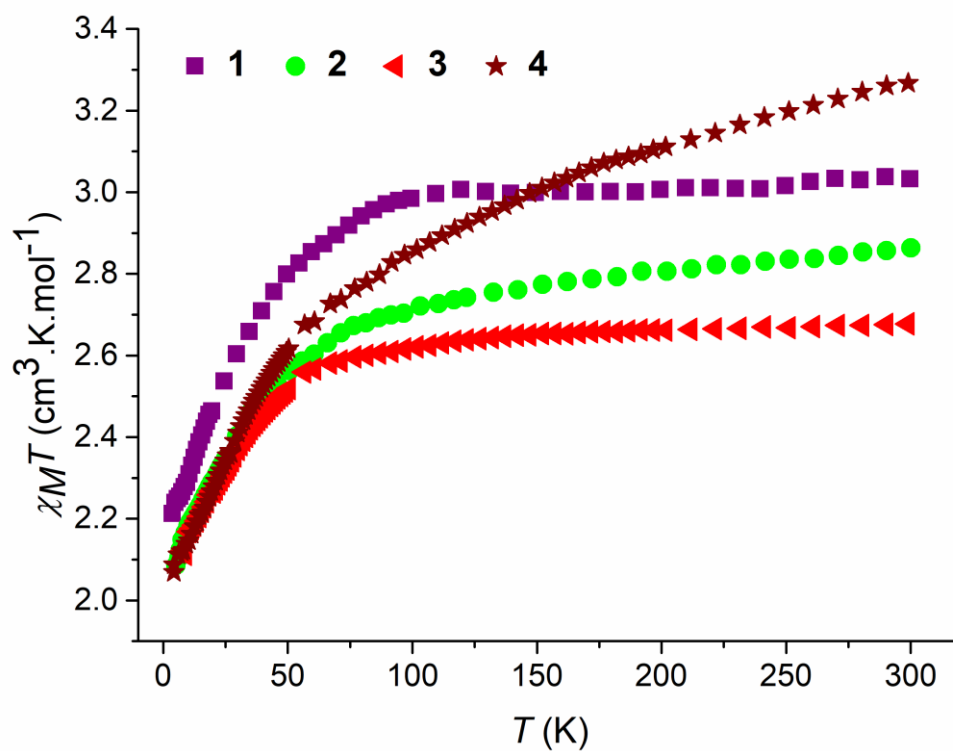
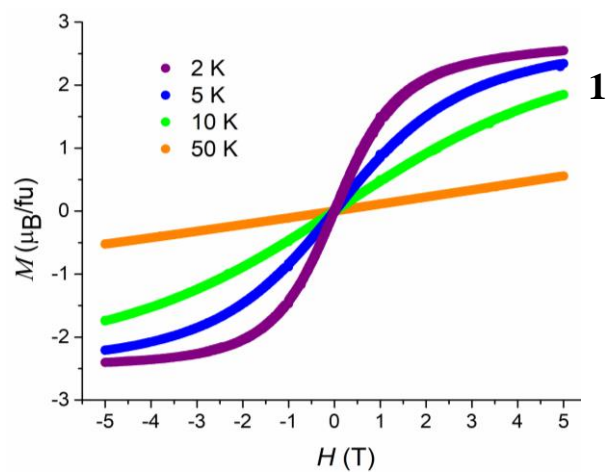
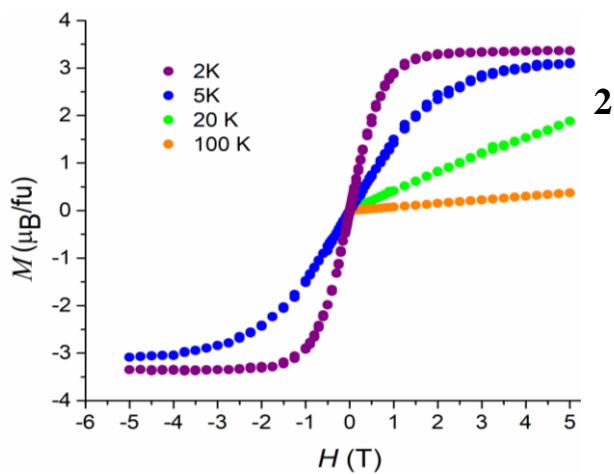


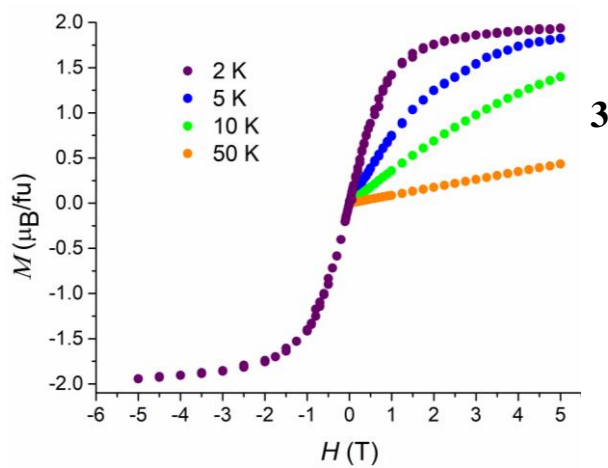
Figure S7. $\chi_M T$ vs T plots measured at 500 G for complexes 1-3 taken from the literature,^{17,18} and comparison with that of complex 4 (this work).



(a)



(b)



(c)

Figure S8. M vs. H plot measured from 0 to 5 T at different temperatures for complexes: (a) **1**, (b) **2** and (c) **3**.

High-Frequency EPR (HFEPR) of complexes 1-4

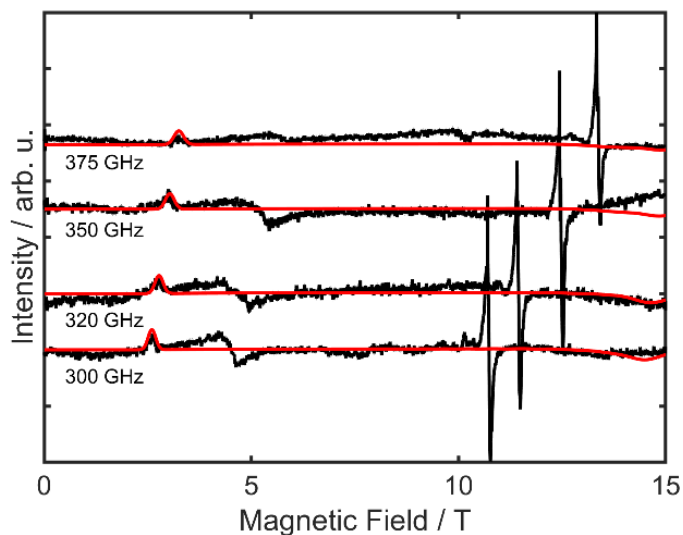


Figure S9. HFEPR spectra of a pressed powder pellet of complex **1** at $T = 5$ K and different frequencies as indicated. Black lines represent the measurement, red lines the simulation on the basis of the spin Hamiltonian parameters given in the main text. The strong resonance line at fields higher than 10 T is due to an instrumental artefact.

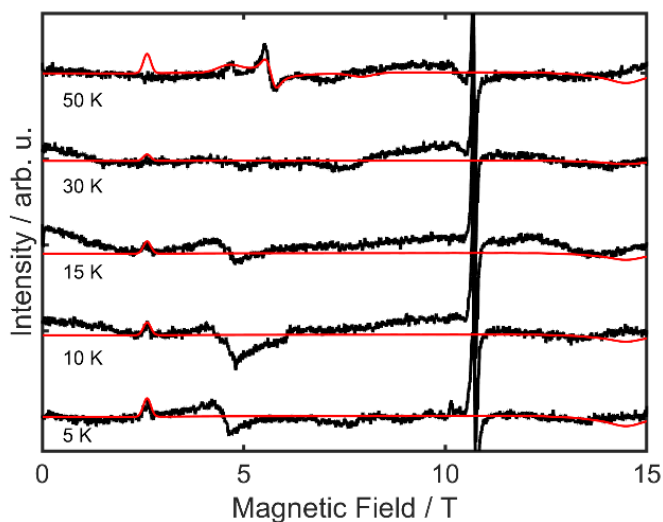


Figure S10. HFEPR spectra of a pressed powder pellet of complex **1** at $\nu = 300$ GHz and different temperatures as indicated. Black lines represent the measurement, red lines the simulation on the basis of the spin Hamiltonian parameters given in the main text. The strong resonance line at fields higher than 10 T is due to an instrumental artefact.

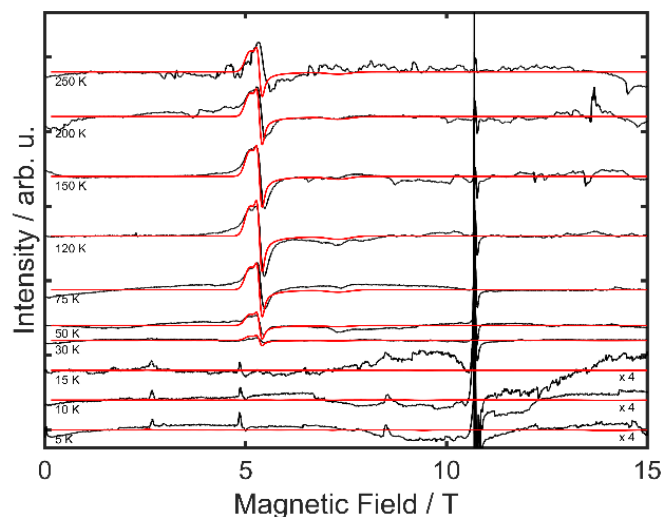


Figure S11. HFEPR spectra of a pressed powder pellet of complex **2** at $\nu = 300$ GHz and different temperatures as indicated. Black lines represent the measurement, red lines the simulation on the basis of the spin Hamiltonian parameters given in the main text. The strong resonance line at fields higher than 10 T is due to an instrumental artefact.

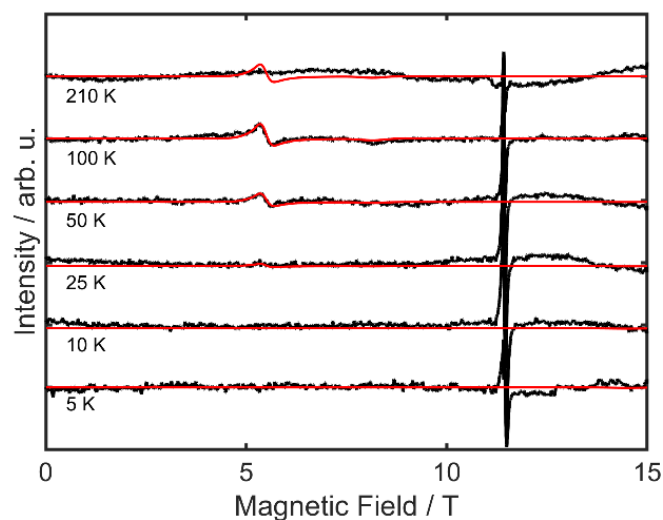


Figure S12. HFEPR spectra of a pressed powder pellet of complex **3** at $\nu = 320$ GHz and different temperatures as indicated. Black lines represent the measurement, red lines the simulation on the basis of the spin Hamiltonian parameters given in the main text. The strong resonance line at fields higher than 10 T is due to an instrumental artefact.

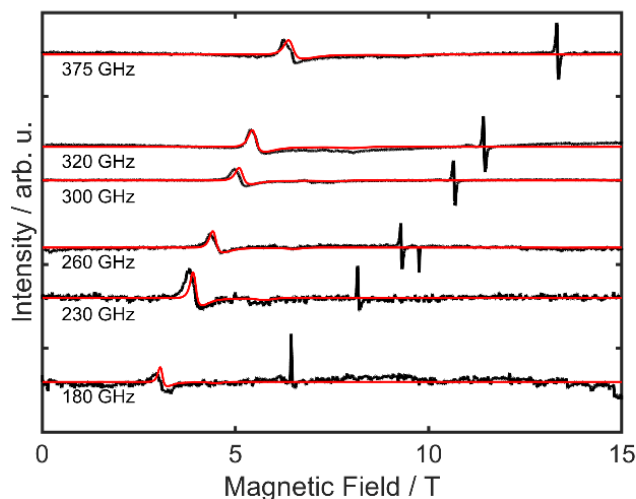


Figure S13. HFEPR spectra of a pressed powder pellet of complex **4** at $T = 50$ K and different frequencies as indicated. Black lines represent the measurement, red lines the simulation on the basis of the spin Hamiltonian parameters given in the main text. The strong resonance line at fields higher than 10 T is due to an instrumental artefact.

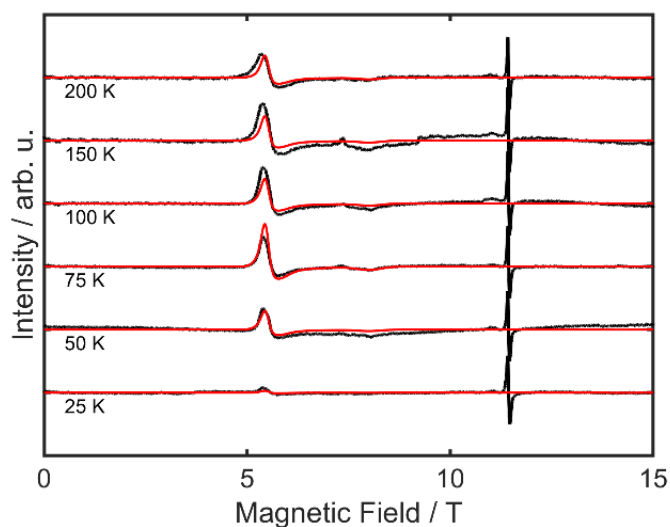


Figure S14. HFEPR spectra of a pressed powder pellet of complex **4** at $\nu = 320$ GHz and different temperatures as indicated. Black lines represent the measurement, red lines the simulation on the basis of the spin Hamiltonian parameters given in the main text. The strong resonance line at fields higher than 10 T is due to an instrumental artefact.

Computational analysis

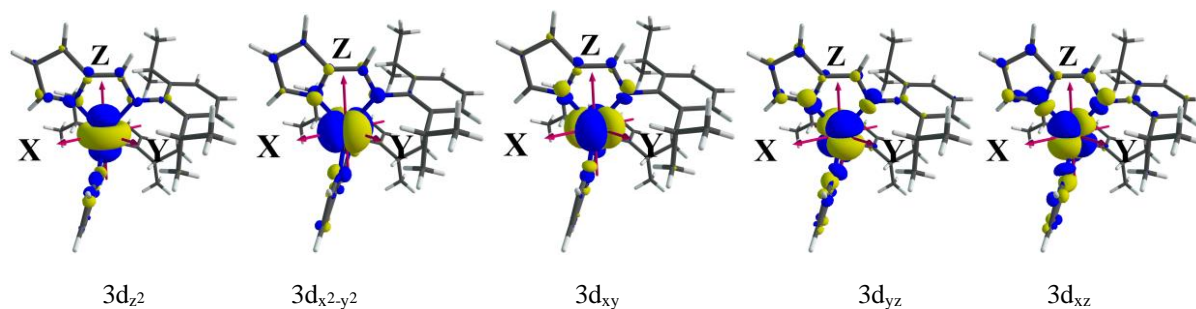


Figure S15. Active space orbitals of complex **1** shown in their magnetic axis frame.

Table S4. Nature of the spin free electronic states of the four complexes and their respective energies.

Complex	State	Configuration State Functions	E (QD-NEVPT2)/cm ⁻¹
1 (#1)	$^4\tilde{X}$	94% $ (3d_{z^2})^2 (3d_{x^2-y^2})^2 (3d_{xy})^1 (3d_{yz})^1 (3d_{xz})^1\rangle$	0
	$^4\tilde{A}$	93% $ (3d_{z^2})^2 (3d_{x^2-y^2})^1 (3d_{xy})^2 (3d_{yz})^1 (3d_{xz})^1\rangle$	1092.3
	$^4\tilde{B}$	71% $ (3d_{z^2})^1 (3d_{x^2-y^2})^2 (3d_{xy})^1 (3d_{yz})^2 (3d_{xz})^1\rangle$ 24% $ (3d_{z^2})^2 (3d_{x^2-y^2})^1 (3d_{xy})^1 (3d_{yz})^2 (3d_{xz})^1\rangle$	6506.6
1 (#2)	$^4\tilde{X}$	94% $ (3d_{z^2})^2 (3d_{x^2-y^2})^2 (3d_{xy})^1 (3d_{yz})^1 (3d_{xz})^1\rangle$	0
	$^4\tilde{A}$	92% $ (3d_{z^2})^2 (3d_{x^2-y^2})^1 (3d_{xy})^2 (3d_{yz})^1 (3d_{xz})^1\rangle$	1076.6
	$^4\tilde{B}$	70% $ (3d_{z^2})^1 (3d_{x^2-y^2})^2 (3d_{xy})^1 (3d_{yz})^2 (3d_{xz})^1\rangle$ 24% $ (3d_{z^2})^2 (3d_{x^2-y^2})^1 (3d_{xy})^1 (3d_{yz})^2 (3d_{xz})^1\rangle$	6893.7
2	$^4\tilde{X}$	97% $ (3d_{z^2})^2 (3d_{x^2-y^2})^2 (3d_{xy})^1 (3d_{yz})^1 (3d_{xz})^1\rangle$	0
	$^4\tilde{A}$	97% $ (3d_{z^2})^2 (3d_{x^2-y^2})^1 (3d_{xy})^2 (3d_{yz})^1 (3d_{xz})^1\rangle$	1369.0
	$^4\tilde{B}$	71% $ (3d_{z^2})^1 (3d_{x^2-y^2})^2 (3d_{xy})^1 (3d_{yz})^2 (3d_{xz})^1\rangle$ 25% $ (3d_{z^2})^2 (3d_{x^2-y^2})^1 (3d_{xy})^1 (3d_{yz})^2 (3d_{xz})^1\rangle$	6813.9
3	$^4\tilde{X}$	95% $ (3d_{z^2})^2 (3d_{x^2-y^2})^2 (3d_{xy})^1 (3d_{yz})^1 (3d_{xz})^1\rangle$	0
	$^4\tilde{A}$	96% $ (3d_{z^2})^2 (3d_{x^2-y^2})^1 (3d_{xy})^2 (3d_{yz})^1 (3d_{xz})^1\rangle$	1576.9
	$^4\tilde{B}$	66% $ (3d_{z^2})^1 (3d_{x^2-y^2})^2 (3d_{xy})^1 (3d_{yz})^2 (3d_{xz})^1\rangle$ 27% $ (3d_{z^2})^2 (3d_{x^2-y^2})^1 (3d_{xy})^1 (3d_{yz})^2 (3d_{xz})^1\rangle$	6786.5
4	$^4\tilde{X}$	98% $ (3d_{z^2})^2 (3d_{x^2-y^2})^2 (3d_{xy})^1 (3d_{yz})^1 (3d_{xz})^1\rangle$	0
	$^4\tilde{A}$	98% $ (3d_{z^2})^2 (3d_{x^2-y^2})^1 (3d_{xy})^2 (3d_{yz})^1 (3d_{xz})^1\rangle$	1460.1
	$^4\tilde{B}$	56% $ (3d_{z^2})^1 (3d_{x^2-y^2})^2 (3d_{xy})^1 (3d_{yz})^2 (3d_{xz})^1\rangle$ 34% $ (3d_{z^2})^2 (3d_{x^2-y^2})^1 (3d_{xy})^1 (3d_{yz})^2 (3d_{xz})^1\rangle$	7263.9

Table S5. Calculated and experimental *g* values.

Complex	<i>g</i>-tensor	
	Calc.	Exp.
1	2.068, 2.120, 2.906 ^{<i>a</i>}	2.05(5), 2.22(2), 2.77(5)
	2.061, 2.107, 2.908 ^{<i>b</i>}	
2	2.088, 2.133, 2.778	2.05(5), 2.05(5), 2.91(2)
3	2.117, 2.143, 2.702	2.10(3), 2.17(3), 2.80(5)
4	2.102, 2.126, 2.739	2.00(5), 2.15(5), 2.85 (5)

^{*a*} Molecule #1 of the unit cell of **1**; ^{*b*} Molecule #2 of the unit cell of **1**.

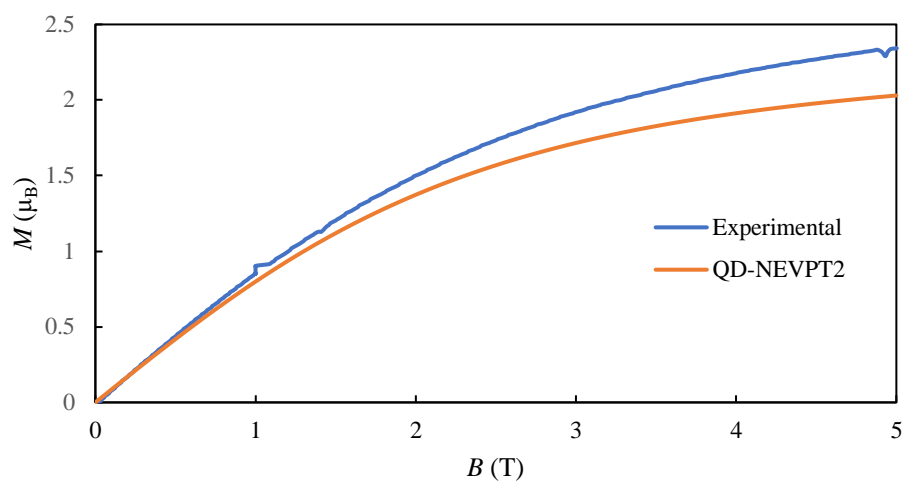


Figure S16. Measured and calculated magnetization, M , vs. B for complex **1**.

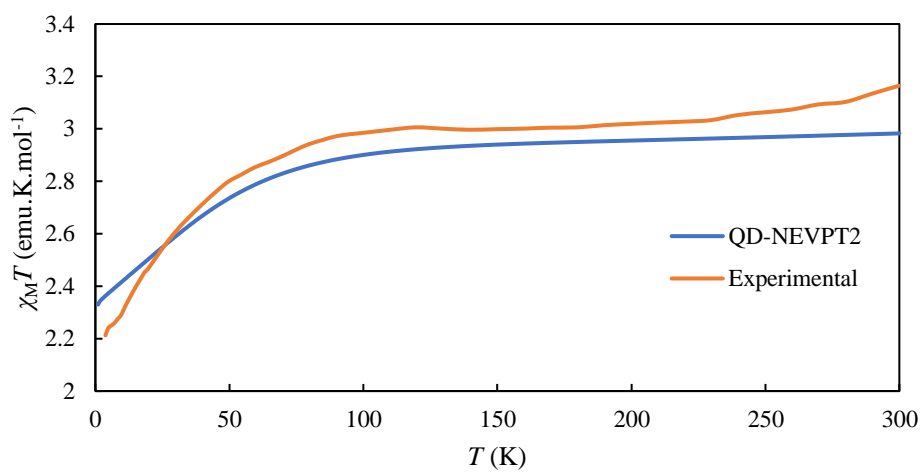


Figure S17. Measured and calculated magnetic susceptibility, $\chi_M T$, vs. T for complex **1**.

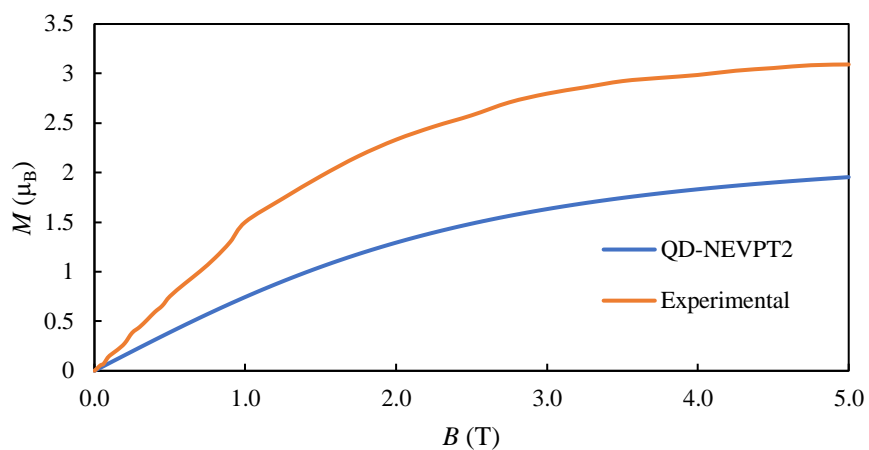


Figure S18. Measured and calculated magnetization, M , vs. B for complex **2**.

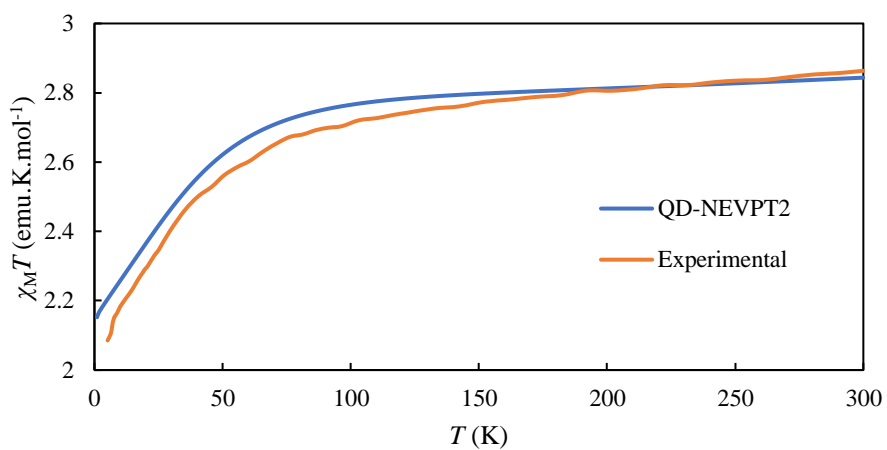


Figure S19. Measured and calculated magnetic susceptibility, $\chi_M T$, vs. T for complex **2**.

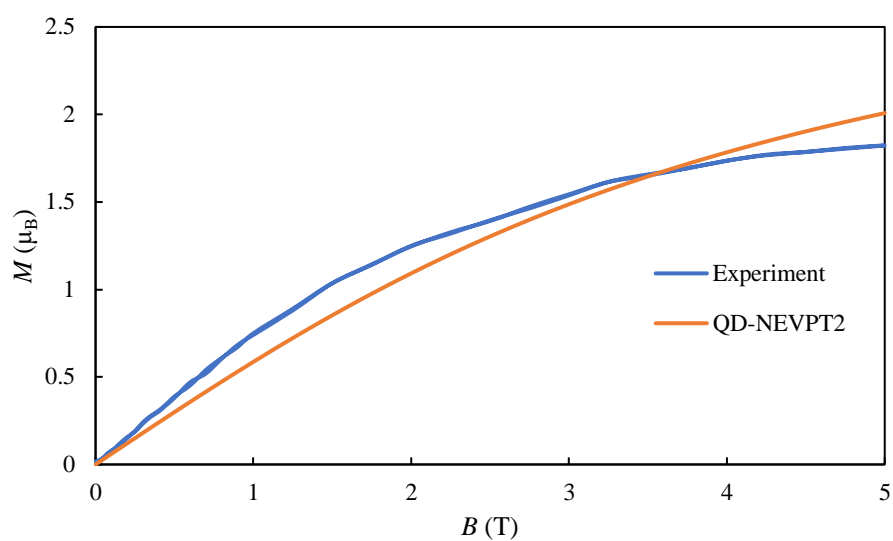


Figure S20. Measured and calculated magnetization, M , vs. B for complex **3**.

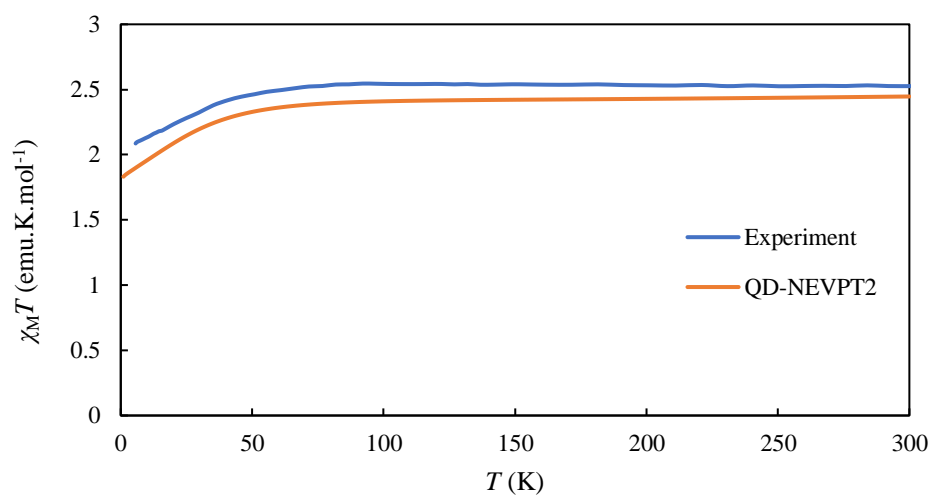


Figure S21. Measured and calculated magnetic susceptibility, $\chi_M T$, vs. T for complex **3**.

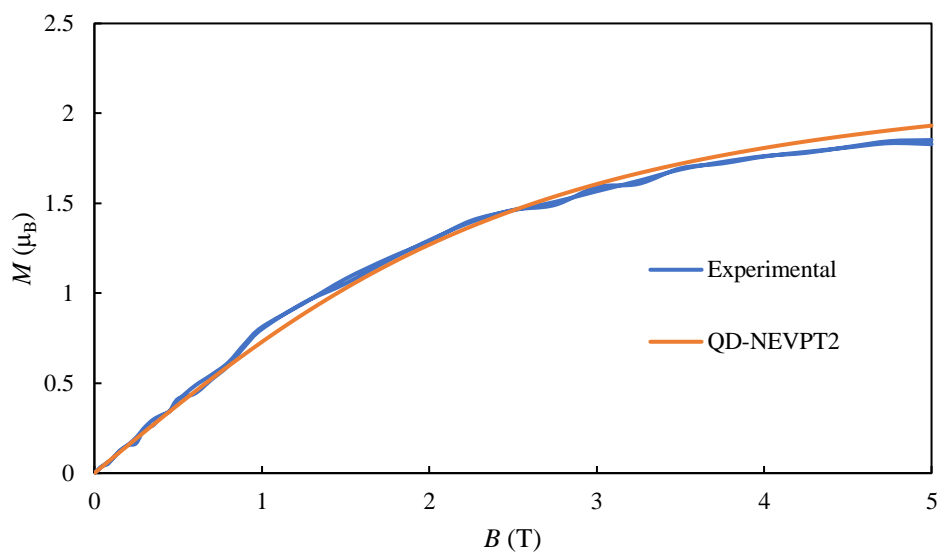


Figure S22. Measured and calculated magnetization, M , vs. B for complex **4**.

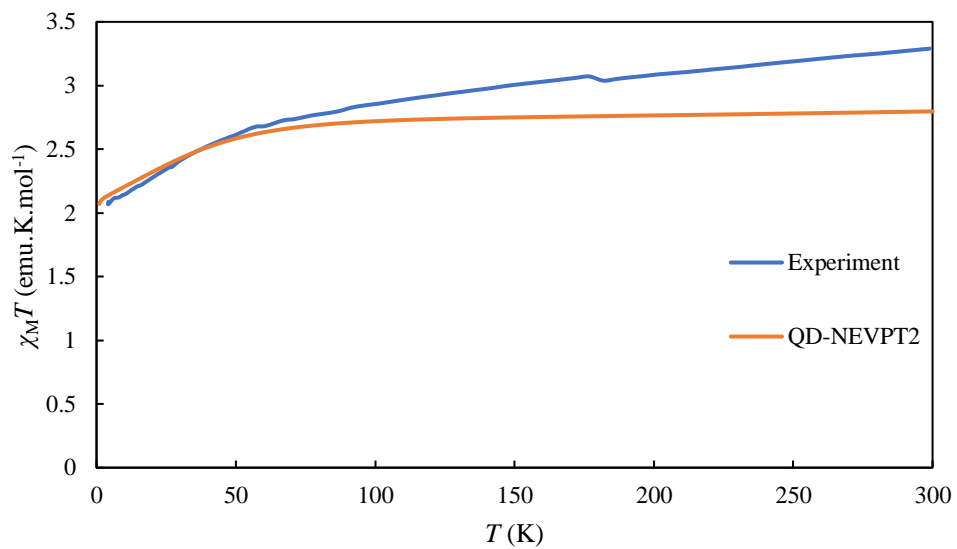


Figure S23. Measured and calculated magnetic susceptibility, $\chi_M T$, vs. T for complex **4**.

Dynamic (ac) magnetic measurements for complexes 1-3

Complex 1

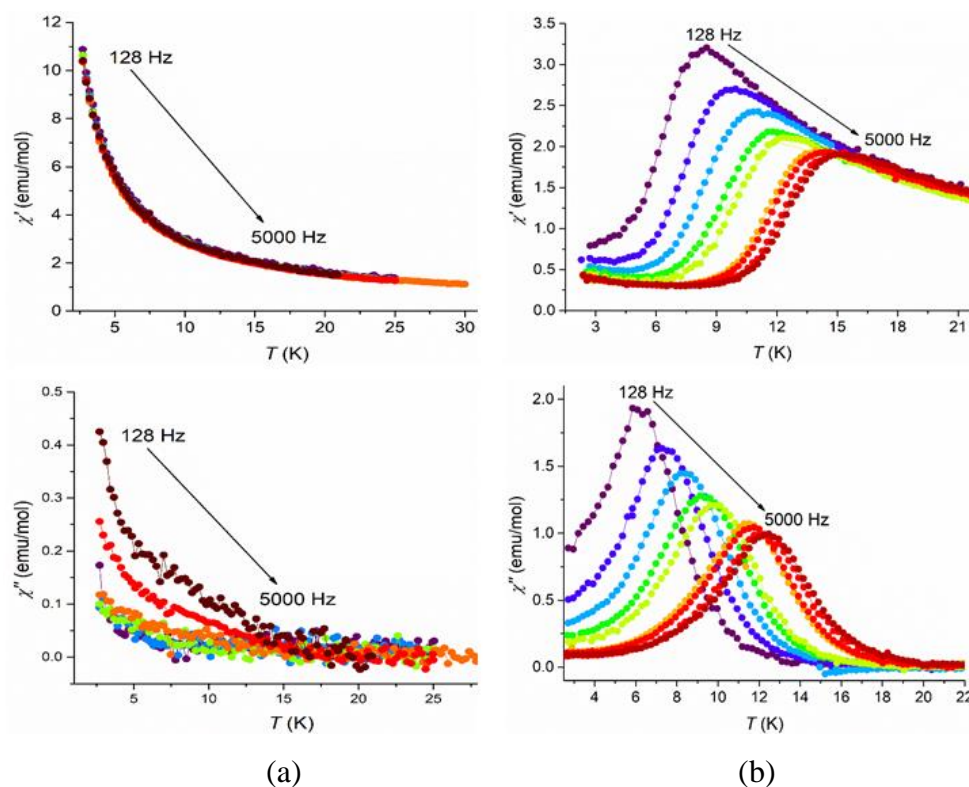


Figure S24. Temperature-dependence of the in-phase, χ' , and out-of-phase, χ'' , magnetic susceptibilities at several different frequencies for complex **1** under (a) zero dc field and (b) 3000 G.

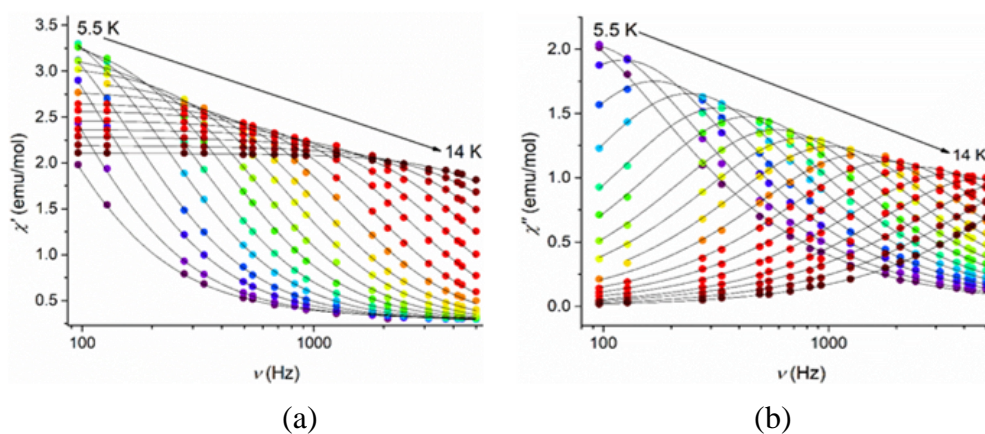


Figure S25. Frequency-dependence of the (a) in-phase, χ' , and (b) out-of-phase, χ'' , magnetic susceptibilities at several different temperatures for complex **1** under a dc field of 3000 G. The solid lines are for guidance.

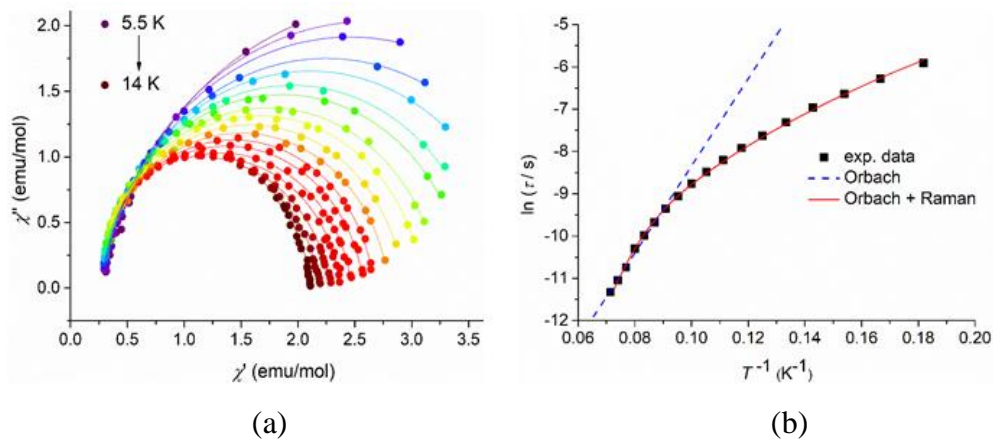


Figure S26. (a) Cole-Cole plot for complex **1** under a dc field of 3000 G. The solid lines represent the best fits to the experimental data using the generalized Debye model. (b) $\ln(\tau)$ vs. T^{-1} plot for **1** under 3000 G. The red line is the fit to the sum of Raman and Orbach processes with $C = 0.086(9) \text{ K}^{-n} \text{ s}^{-1}$, $n = 4.86(5)$, $U_{eff} = 138 \text{ cm}^{-1}$ (fixed) and $\tau_0 = 1.14(6) \times 10^{-11} \text{ s}$ and the dashed blue line is the fit of the Orbach process using the Arrhenius law with $U_{eff} = 76(4) \text{ cm}^{-1}$ and $\tau_0 = 5.1(3) \times 10^{-9} \text{ s}$.

Complex 2

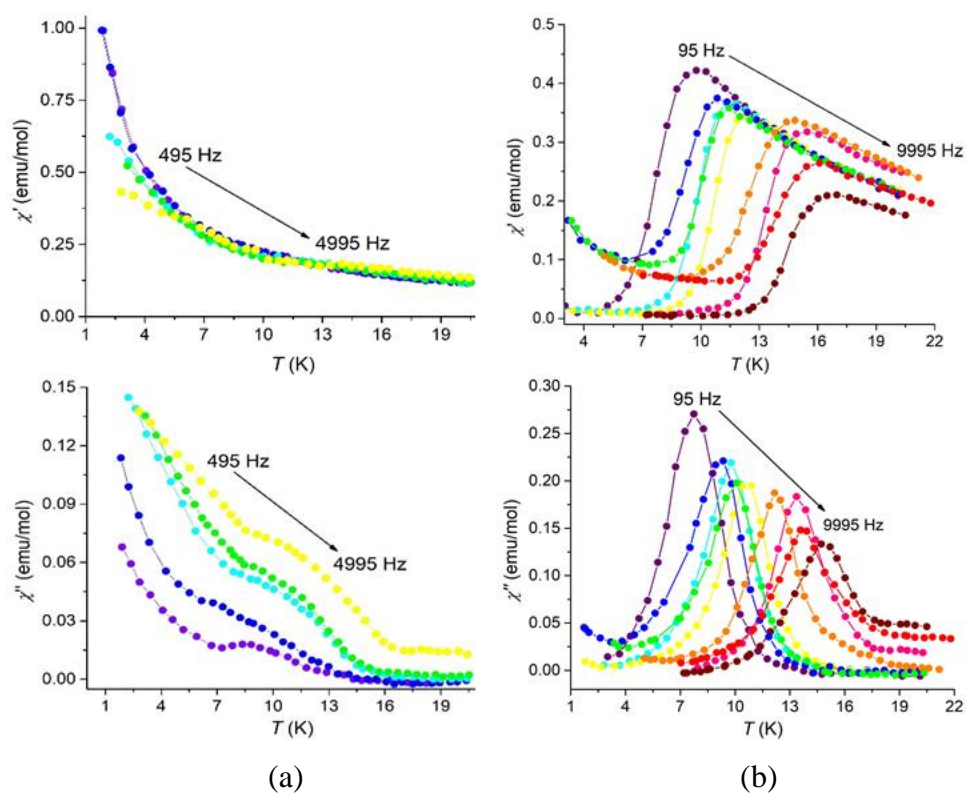


Figure S27. Temperature-dependence of the in-phase, χ' , and out-of-phase, χ'' , magnetic susceptibilities at several different frequencies for complex **2** under (a) zero dc field and (b) 1000 G.

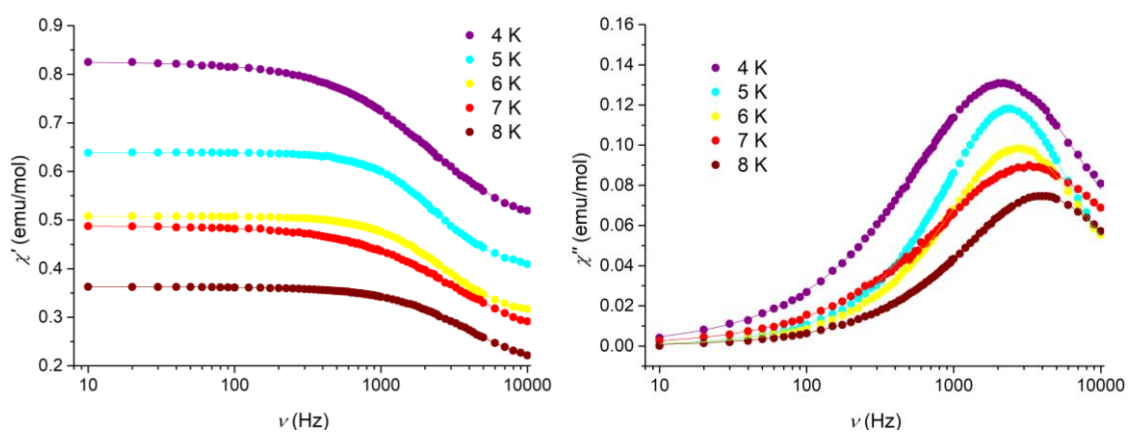


Figure S28. Frequency-dependence of the (a) in-phase, χ' , and (b) out-of-phase, χ'' , magnetic susceptibilities at several different temperatures for complex **2** under zero dc field. The solid lines are for guidance.

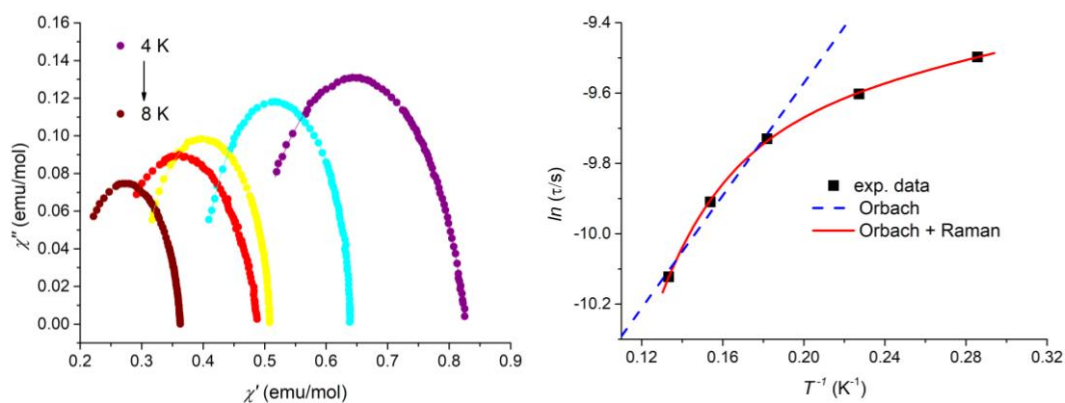


Figure S29. (a) Cole-Cole plot for complex **2** in the absence of an external magnetic field. The solid lines represent the best fits to the experimental data using the generalized Debye model. (b) $\ln(\tau)$ vs. T^{-1} plot for **2** in the absence of an external magnetic field. The red line is the fit to the sum of Raman and Orbach processes with $C = 0.98(9) \text{ K}^{-n} \text{ s}^{-1}$, $n = 4.5(5)$, $U_{\text{eff}} = 0.77(2) \text{ cm}^{-1}$ and $\tau_0 = 5.6(4) \times 10^{-5} \text{ s}$ and the dashed blue line is the fit of the Orbach process using the Arrhenius law with $U_{\text{eff}} = 8(1) \text{ cm}^{-1}$ and $\tau_0 = 1.4(2) \times 10^{-5} \text{ s}$.

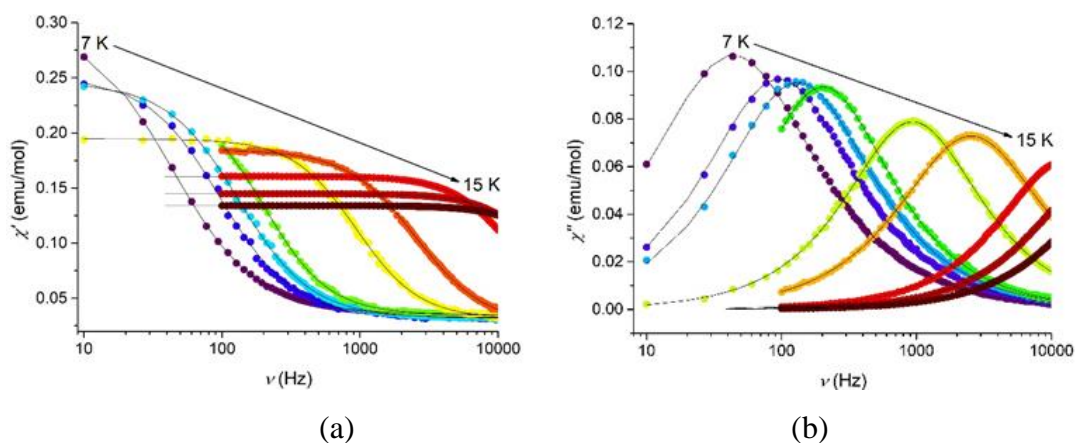


Figure S30. Frequency-dependence of the (a) in-phase, χ' , and (b) out-of-phase, χ'' , magnetic susceptibilities at several different temperatures for complex **2** under a dc field of 1000 G. The solid lines are for guidance.

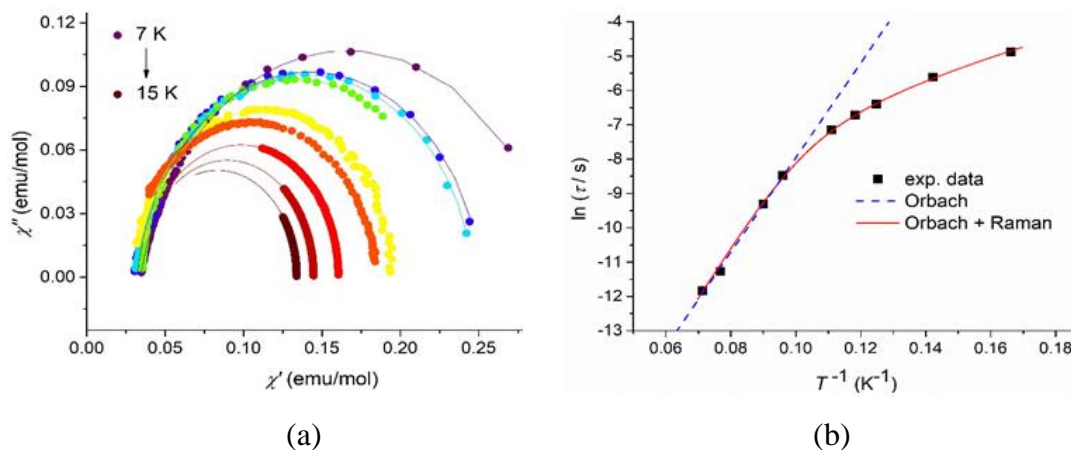


Figure S31. (a) Cole-Cole plot for complex **2** under a dc field of 1000 G. The solid lines represent the best fits to the experimental data using the generalized Debye model. (b) $\ln(\tau)$ vs. T^{-1} plot for **2** under 1000 G. The red line is the fit to the sum of Raman and Orbach processes with $C = 0.02(3) \text{ K}^{-n} \text{ s}^{-1}$, $n = 4.9(7)$, $U_{eff} = 106 \text{ cm}^{-1}$ (fixed) and $\tau_0 = 1.3(2) \times 10^{-10} \text{ s}$ and the dashed blue line is the fit of the Orbach process using the Arrhenius law with $U_{eff} = 90.6(5) \text{ cm}^{-1}$ and $\tau_0 = 6.0(4) \times 10^{-10} \text{ s}$.

Complex 3

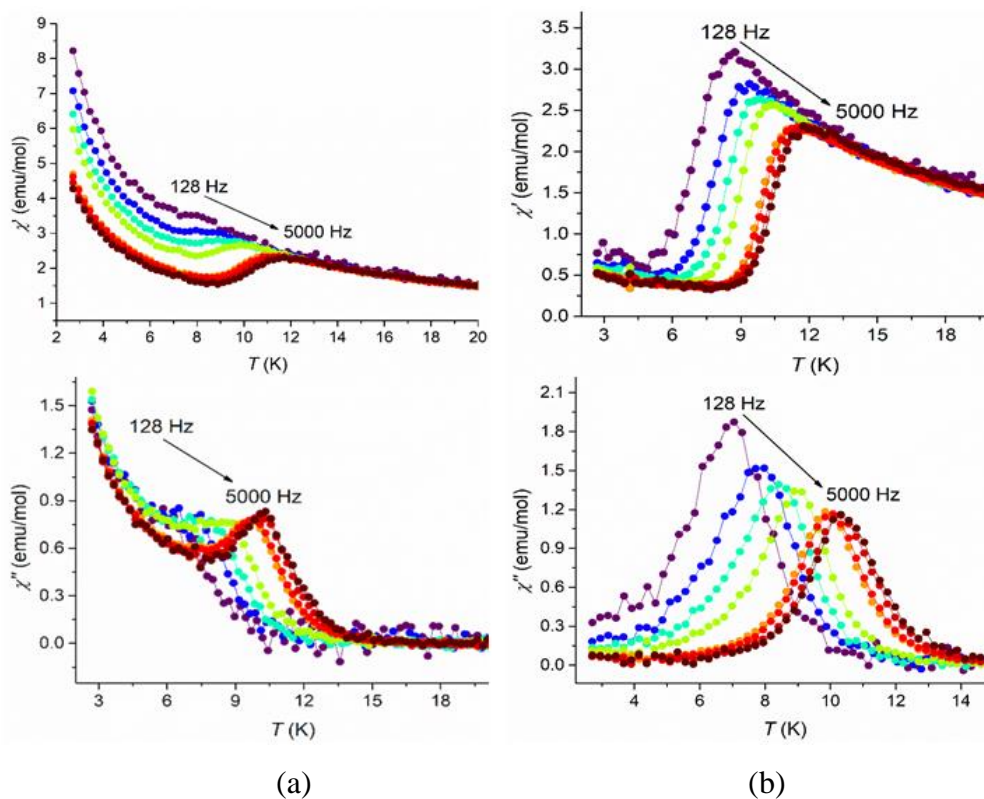


Figure S32. Temperature-dependence of the in-phase, χ' , and out-of-phase, χ'' , magnetic susceptibilities at several different frequencies for complex **3** under (a) zero dc field and (b) 800 G.

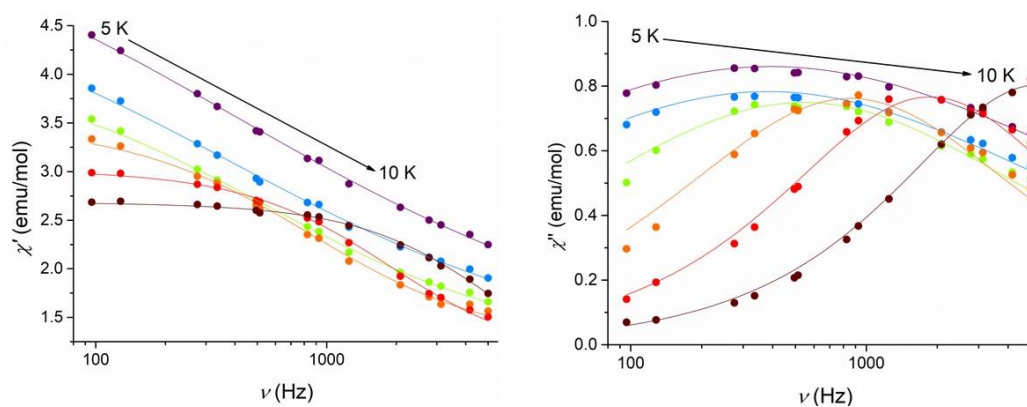
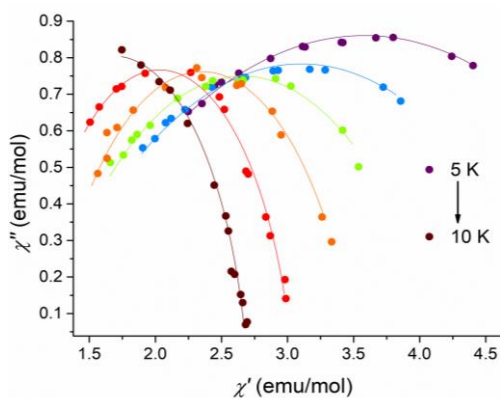
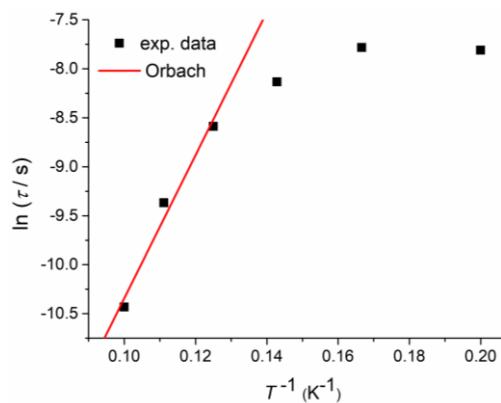


Figure S33. Frequency-dependence of the (a) in-phase, χ' , and (b) out-of-phase, χ'' , magnetic susceptibilities at several different temperatures for complex **3** under zero dc field. The solid lines are for guidance.



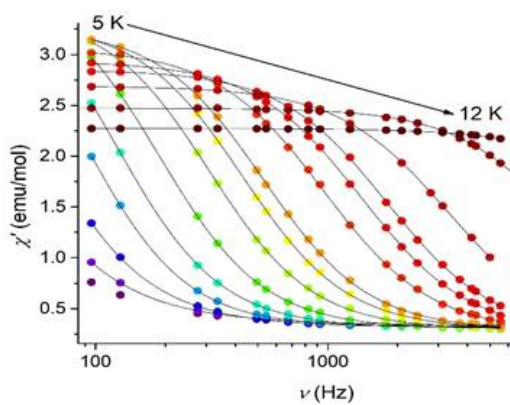
(a)



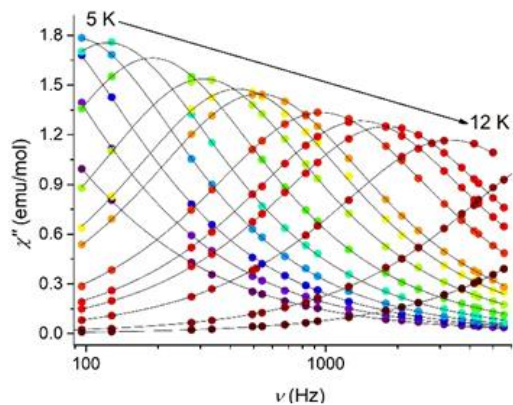
(b)

Figure S34. (a) Cole-Cole plot for complex **3** in the absence of an external magnetic field. The solid lines represent the best fits to the experimental data using the generalized Debye model. (b) $\ln(\tau)$ vs. T^{-1} plot for **3** in the absence of an external magnetic field; the red line is the fit for the Orbach process using the Arrhenius law

$$\text{with } U_{\text{eff}} = 51(11) \text{ cm}^{-1} \text{ and } \tau_0 = 2.2(1) \times 10^{-8} \text{ s}$$

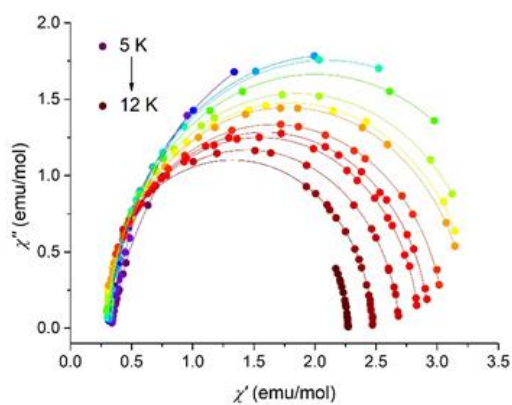


(a)

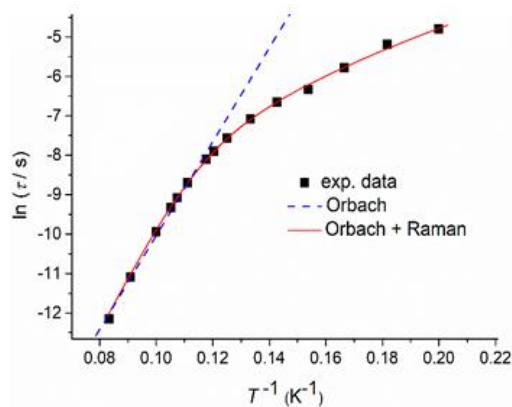


(b)

Figure S35. Frequency-dependence of the (a) in-phase, χ' , and (b) out-of-phase, χ'' , magnetic susceptibilities at several different temperatures for complex **3** under a dc field of 800 G. The solid lines are for guidance.



(a)



(b)

Figure S36. (a) Cole-Cole plot for complex **3** under a dc field of 800 G. The solid lines represent the best fits to the experimental data using the generalized Debye model. (b) $\ln(\tau)$ vs. T^{-1} plot for **3** under 800 G. The red line is the fit to the sum of Raman and Orbach processes with $C = 0.021(4) \text{ K}^{-n} \text{ s}^{-1}$, $n = 5.54(1)$, $U_{\text{eff}} = 96 \text{ cm}^{-1}$ (fixed) and $\tau_0 = 6.8(2) \times 10^{-11} \text{ s}$ and the dashed blue line is the fit of the Orbach process using the Arrhenius law with $U_{\text{eff}} = 88(3) \text{ cm}^{-1}$ and $\tau_0 = 1.5(3) \times 10^{-10} \text{ s}$.

Complex 4

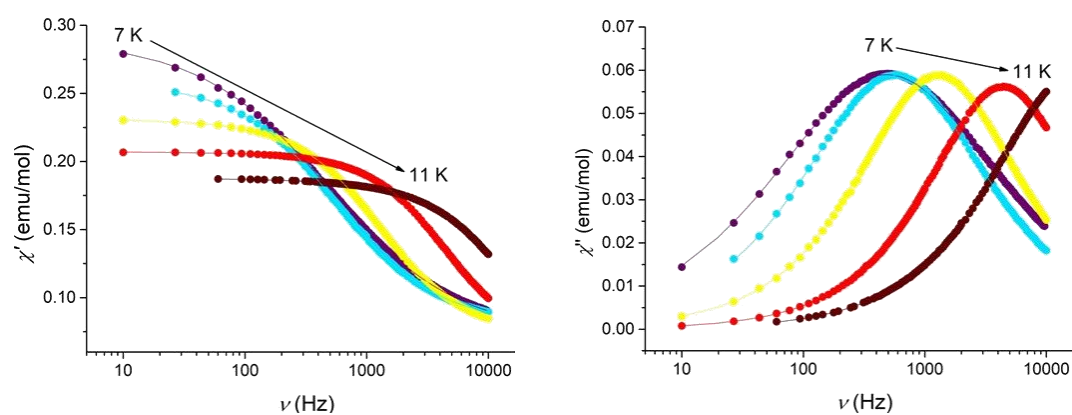


Figure S37. Frequency-dependence of the (a) in-phase, χ' , and (b) out-of-phase, χ'' , magnetic susceptibilities at several different temperatures for complex 4 under zero dc field. The solid lines are for guidance.

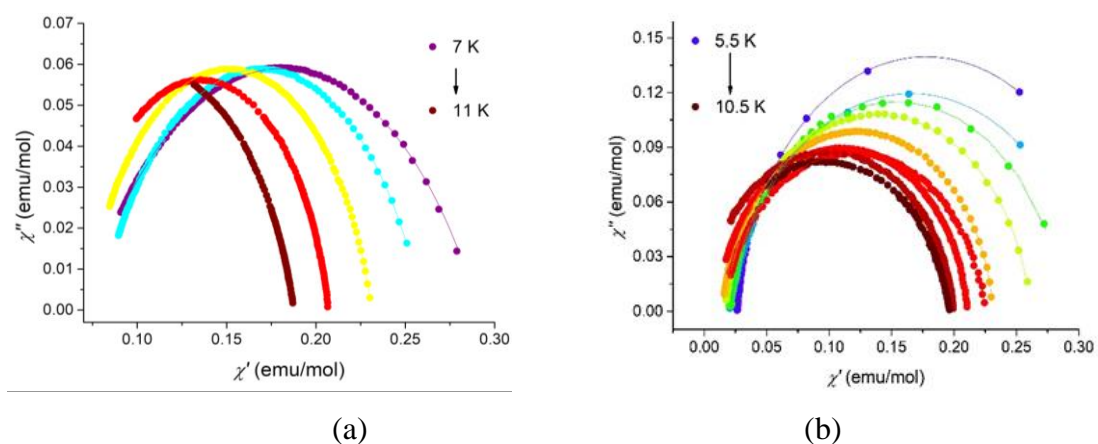


Figure S38. (a) Cole-Cole plot for complex 4 in the absence of an external magnetic field. (b) Cole-Cole plot for complex 4 under a field of 800 G. The solid lines represent the best fits to the experimental data using the generalized Debye model.